Advances in Industrial and Manufacturing Engineering 12 (2026) 100184

Contents lists available at ScienceDirect

Advances in Industrial and Manufacturing Engineering

journal homepage: www.elsevier.com/locate/aime

Regular aricles

Experimental–numerical investigation of force-controlled friction extrusion process via feedback-controlled simulation

Ahmed Elbossily [a,*], Zina Kallien [a,b], Lars Rath [b], Rupesh Chafle [b], Mohamadreza Afrasiabi [c], Benjamin Klusemann [a,b]

[a] Institute for Production Technology and Systems, Leuphana Universität Lüneburg, Universitätsallee 1, 21335, Lüneburg, Germany
[b] Institute of Material and Process Design, Helmholtz-Zentrum Hereon, Max–Planck-Straße 1, 21502 Geesthacht, Germany
[c] Advanced Manufacturing Lab, ETH Zurich, Zurich, Switzerland

ARTICLE INFO

Dataset link: https://github.com/SPH-SSMP/FE-SPH-GPU, https://doi.org/10.5281/zenodo.18657543

Keywords:
Friction extrusion
Process modeling
Experimental investigation
Temperature field
Material flow

ABSTRACT

Friction extrusion is an emerging solid-state manufacturing technique for producing rods and tubes, but ensuring uniform microstructural properties along the extrudate length remains a major challenge. This work introduces, for the first time, a feedback-controlled friction extrusion framework in which high-fidelity smoothed particle hydrodynamics (SPH) simulations are coupled with a proportional–integral–derivative (PID) controller to regulate the force-controlled process numerically. Unlike existing numerical approaches that rely on experimentally prescribed die displacement or velocity profiles, the proposed PID–SPH framework allows die displacement to evolve naturally in response to material resistance while maintaining a prescribed extrusion force. The framework is implemented in a GPU-accelerated SPH solver, enabling fast and efficient simulation of the nonlinear thermomechanical behavior inherent to friction extrusion. The PID-SPH framework is validated against experiments on the extrusion of 14 mm rods from high-strength AA7075-T6 billets using a flat die, with comparisons in extrusion force, die plunging displacement, and temperature evolution. Thirteen thermocouples positioned at different radii and depths provided detailed thermal data at the die–billet interface and within the billet during the process. The results demonstrate that the PID–SPH framework accurately captures the force-controlled thermomechanical response of friction extrusion. Beyond predictive accuracy, the framework provides insight into the origin of microstructural nonuniformity along the extrudate length by resolving the coupled evolution of strain rate, material flow, and thermal fields under applied force. These insights support the identification of key factors governing grain size variation and the evaluation of mitigation strategies, such as controlled thermal management, to promote more uniform microstructural development.

1. Introduction

Friction extrusion (FE) is a solid-state manufacturing process used for producing high-strength wires, rods, tubes, and other profiles (Feng et al., 2023). In this process, a rotating die is pressed against a contained feedstock material. Friction between the die and feedstock, along with plastic deformation of the feedstock, generates heat that softens the material, which is then forced through an orifice in the die to form the extrudate. The FE process generally consists of two phases: heating and extrusion. During heating, the die rotates at high speed with minimal plunging, generating heat without material flow. The extrusion phase follows, characterized by reduced die speed and increased feed rate, which drives the softened material through the die orifice in the solid state. This avoids solidification-related defects such as alloy segregation, shrinkage, and gas porosity (Ghosh, 2001). Under the thermomechanical conditions of severe plastic deformation at elevated temperatures, a substantial fraction of the extruded material undergoes dynamic recrystallization, producing refined grains that enhance mechanical strength and performance (Akar et al., 2022). As a result, FE is particularly effective for manufacturing tubes (Whalen et al., 2019), while mitigating tearing and cracking in the extrudate (Saha, 1998). Moreover, the process can accommodate a wide range of feedstock materials (including aluminum alloys (Tang and Reynolds, 2010), magnesium alloys (Baffari et al., 2017b), and composites (Li et al., 2021b)) in various forms such as chips (Baffari et al., 2017a), powders (Dhoka et al., 2021), and billets (Cho et al., 2014), making it an attractive technology for diverse industrial applications.

Combining experimental work with numerical simulations is essential for gaining deeper insights into FE process. For instance, Chen

* Corresponding author.
E-mail address: Ahmed.Elbossily@leuphana.de (A. Elbossily).

https://doi.org/10.1016/j.aime.2026.100184
Received 27 November 2025; Received in revised form 8 February 2026; Accepted 8 February 2026
Available online 9 February 2026

et al. (2009) employed a 2D FEM model to study the effects of die angle, friction, and orifice radius, while Behnagh et al. (2015) coupled 2D FEM simulations with experiments to investigate microstructural evolution during chip-based FE. However, both studies relied on 2D simplifications, which limited their ability to capture the complex 3D material flow inherent to the process. Baffari et al. (2017c) advanced to 3D FEM modeling for force-controlled FE of 5 mm wire, but their approach required experimentally measured die plunging velocity as a direct input to the simulation, reducing the model's predictive capability by depending on prior experimental data. Similarly, Zhang et al. (2018) developed a 3D CFD model for 2.54 mm wire extrusion, but again relied on measured die displacement data to define the die's vertical motion in the simulation.

In addition to the FEM and CFD models, the smoothed particle hydrodynamics (SPH) method (Fraga Filho et al., 2019) has been employed in the analysis of the FE process. SPH is highly effective in managing large material deformations and mixing, making it a prominent method for simulating solid-state processes such as friction stir welding (FSW) (Bagheri et al., 2020), additive friction stir deposition (AFSD) (Stubblefield et al., 2021), and friction surfacing (FS) (Jamshidi Aval, 2021). Li et al. (2021a) developed a 3D, fully thermomechanically coupled SPH model to simulate FE of 2.54 mm wire in a displacement-controlled experiment. The model was successfully validated against experimental results, demonstrating the effectiveness of the SPH model in simulating the FE process. However, since the simulation was run on a CPU, it required 52 hours to simulate 50 seconds of the FE process, highlighting computational efficiency limitations. In subsequent work, Li et al. (2022, 2024) extended the model to simulate FE of tubes and integrated a dislocation density-based constitutive model to enhance predictive capabilities. While the improvements advanced model fidelity, the simulations remained computationally demanding, requiring 216 hours on a supercomputer.

Despite advances in numerical modeling of friction extrusion, some gaps remain. Most studies focus on producing wires under 5 mm in diameter, overlooking the potential for larger-diameter rods. This limits insight into applications like solid-state material deposition, such as friction surfacing (Aspes et al., 2025) or AFSD, where larger rods are essential. Moreover, current numerical models for simulating force-controlled friction extrusion process rely on experimentally measured die plunging velocity profiles as direct simulation inputs, which fundamentally limits their predictive capability—requiring prior experimental data before simulations can be conducted. To date, no framework has been developed to model the force-controlled friction extrusion process directly. Besides that, all existing numerical models suffer from excessively long computation times, which restricts the ability to perform parameter optimization and refine model accuracy.

The primary objective of this study is to enable predictive simulation of force-controlled friction extrusion without reliance on experimentally prescribed die displacement or velocity inputs. To this end, a closed-loop PID controller is integrated directly into a high-fidelity SPH solver, allowing the die displacement to evolve naturally in response to the evolving material resistance in order to maintain a prescribed extrusion force. Beyond predictive capability, the proposed framework is employed to investigate the thermomechanical evolution and material flow during the process, with particular emphasis on identifying the mechanisms responsible for non-uniform grain development along the extrudate length under force-controlled conditions. This analysis provides a basis for evaluating process modifications aimed at mitigating microstructural inhomogeneity along the extrudate length.

2. Experimental setup

In this study, the FE process was carried out using the FE100 (Bond Technologies, IN, USA). A flat-faced die was used to extrude a 14 mm diameter rod from a 50 mm diameter AA7075-T6 billet (extrusion ratio of 12.76). The die and container were made of H13 tool steel and 4140 Cr-Mo steel, respectively. To monitor the die temperature, a K-type thermocouple (Tc) was placed 0.5 mm below the die surface and 16.5 mm from its center, Fig. 1. To obtain a nearly full-field temperature field over time, three experiments were conducted, each using four thermocouples positioned at radial distances of 0 mm, 6.25 mm, 12.5 mm, and 18.75 mm. In each experiment, the thermocouples were placed at different depths relative to the billet top. This arrangement enables analysis of how the billet's temperature varies radially as the die advances. The processes were carried out under force-control mode at room temperature. During the extrusion process, the thermocouples record the process temperature until they are approached by the die and are extruded, leading to failure of the sensor. The remaining thermocouples in the billet and the extrudate act as tracer material, whereas their position can be analyzed using micro-computed tomography (μCT). μCT scans of the remaining billet material (with failed thermocouples) were performed at 117 kV and 103 μA using YCougar SMT equipment (Yxlon International, Germany), where the resolution was 49.3 μm.

Fig. 2 presents exemplarily the recorded die plunging displacement, die plunging velocity, container rotational speed, and extrusion force throughout one process. During the initial 26 seconds heating phase, the container rotates at 300 rpm with a constant applied force of 50 kN. In the following 10 seconds transition phase, the container rotational speed is linearly reduced to 90 rpm, and the extrusion force is increased to 300 kN. Finally, in the extrusion phase, the extrusion force and container rotational speed are stabilized at 300 kN and 90 rpm, respectively.

For referencing purposes, the friction extrusion process has been repeated without additional thermocouples, where samples were cut from the rod as well as from the residual billet material for microstructural analyses. Longitudinal sections were cut from the wire at 0–5 cm and 17–23 cm. The samples were embedded and prepared, following common metallographic practices. Electrochemical etching was performed using Barker's solution at 15 V for 120 seconds. Micrographs of the sections were taken at a light optical microscope (VHX-7000, Keyence, Germany). Hardness mappings were conducted using an automated hardness testing machine (Durascan 70 G5, EMCO-TEST GmbH, Austria) using a load of 0.1 kgf (HV0.1), a holding time of 10 seconds, and an indent spacing of 1 mm.

3. Process modeling

The FE process is mathematically described using the equilibrium condition of continuum mechanics, its mechanical boundary conditions, and the Fourier heat equation with its boundary conditions. The governing system for solid mechanics includes three conservation laws: mass, momentum, and energy, along with constitutive and kinematic equations. The material model utilizes Hooke's law (William D. Callister and Rethwisch, 2020) for elastic deformation and J2 plasticity theory (Borja, 2013) to capture plastic behavior, represented by the Johnson-Cook model (Johnson and Cook, 1983).

The SPH method is used for discretizing the covering equations. SPH method is a mesh-free computational approach that employs kernel interpolation to solve field equations (Fraga Filho et al., 2019). This kernel function operates on a group of nearby particles within a specified distance, determined by a smoothing length h. Through kernel interpolation, the SPH method provides precise approximations of field variables and their derivatives, delivering smooth and continuous results without relying on a structured mesh. For brevity, a detailed description of the discretized governing equations is omitted at this point; the interested reader is referred to Elbossily et al. (2025).

The rest of this section focuses on the contact and friction forces, heat generation and dissipation, PID controller integration, and model setup. For completeness, details on the notation used in this work are provided in Appendix A.

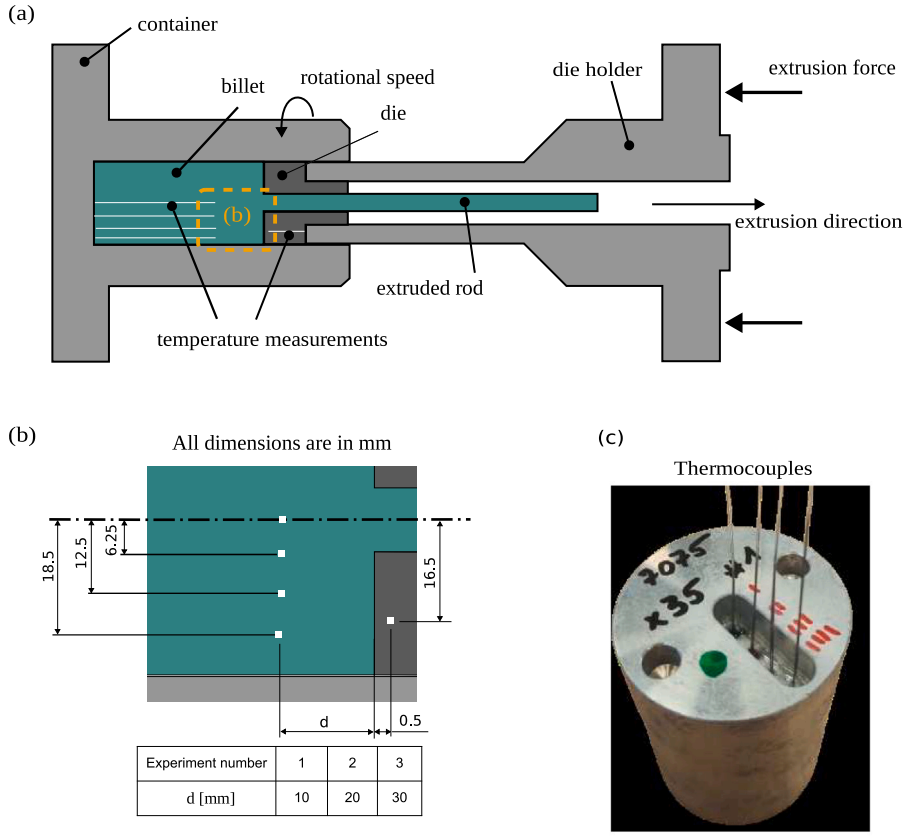

Fig. 1. (a) Schematic of the experimental setup for the FE with temperature measurements in the die and billet. (b) Detailed view of the die and billet section marked with the orange dashed square in (a), illustrating the thermocouple positions relative to the centerline for three experimental sets with different distances d from the billet top. (c) Photograph of the billet with inserted thermocouples.

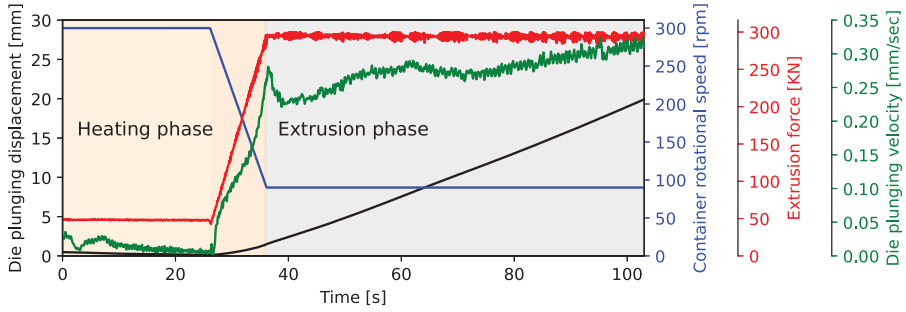

Fig. 2. Die plunging displacement, die plunging velocity, container rotational speed, and extrusion force during a representative friction extrusion process. Data obtained from the extrusion equipment. The initial 26 s represents the heating phase, followed by a 10 s ramping phase until the extrusion phase starts.

3.1. Contact and friction forces

The contact force between a deformable billet particle and the rigid surfaces of the container and die is determined using a penalty-based approach (Stubblefield et al., 2021). The contact force is given by

$$\boldsymbol{f}_{is}^{\text{con}} = [\lambda_1 p_{is} + \lambda_2 \dot{p}_{is}]\boldsymbol{n}_s, \tag{1}$$

where p_{is} and $\dot{p}_{is}$ are the penetration distance and rate, respectively, and $\boldsymbol{n}_s$ is the unit normal of the rigid surface, given by

$$\boldsymbol{n}_s = \begin{cases} (0,0,-1), & \text{die contact surface} \\ \frac{\boldsymbol{r}_i}{\|\boldsymbol{r}_i\|}, & \text{orifice and container contact surfaces} \end{cases} \tag{2}$$

where $\boldsymbol{r}_i$ is the particle's radial unit vector relative to the aligned container and die symmetry axis. λ_1 and λ_1 are calculated as follows

$$\lambda_1 = \frac{P}{2\Delta t^2}, \quad \lambda_2 = D\sqrt{8\lambda_1 m_i^3}, \tag{3}$$

where P and D are penalty and damping factors, respectively. Δt is the simulation time step. The penetration $\dot{p}_{is}$ rate is determined via

$$\dot{p}_{is} = \boldsymbol{v}_{is}^{\text{rel}} \cdot \boldsymbol{n}_s, \tag{4}$$

where the relative velocity $\boldsymbol{v}_{is}^{\text{rel}}$ is

$$\boldsymbol{v}_{is}^{\text{rel}} = \boldsymbol{v}_i - \boldsymbol{v}_s. \tag{5}$$

The rigid surface velocity $\boldsymbol{v}_s$ is given by

$$\boldsymbol{v}_s = \begin{cases} \boldsymbol{w}_{\text{die}} \times \boldsymbol{r}_i + \boldsymbol{v}_{\text{p}}, & \text{die contact surface} \\ \boldsymbol{w}_{\text{die}} \times [\boldsymbol{n}_s r_o] + \boldsymbol{v}_{\text{p}}, & \text{orifice contact surface} \\ \boldsymbol{0}, & \text{container contact surface} \end{cases} \tag{6}$$

where $\boldsymbol{w}_{\text{die}}$ is the angular velocity of the die. $\boldsymbol{v}_{\text{p}}$ is the die plunging velocity, and r_o is the radius of the die orifice.

The Coulomb–Tresca contact condition, suggested by Li et al. (2021a, 2022) for simulating FE process, is applied to distinguish between slipping and sticking conditions. If the friction force, calculated using Coulomb's friction law, exceeds the maximum allowable shear force of the billet material $f^{\text{shear}}_{i,\text{allowable}}$, the material is considered to be sticking to the die, i.e., $\boldsymbol{v}_i = \boldsymbol{v}_s$. The friction force is determined as follows:

$$\boldsymbol{f}^{\text{fric}}_{is} = \min\left(\mu\|\boldsymbol{f}^{\text{con}}_{is}\|, f^{\text{shear}}_{i,\text{allowable}}\right)\frac{\boldsymbol{v}^{\text{rel,t}}_{is}}{\|\boldsymbol{v}^{\text{rel,t}}_{is}\|}, \tag{7}$$

where μ is the friction coefficient. The maximum allowable shear force is given by:

$$f^{\text{shear}}_{i,\text{allowable}} = \frac{\sigma^y_i A^{\text{shear}}_i}{\sqrt{3}}. \tag{8}$$

Here, σ^y_i represents the current yield strength, which is determined using the Johnson-Cook (JC) model. The particle shear area is defined as $A^{\text{shear}}_i = \Delta x^2$. The tangential relative velocity, $\boldsymbol{v}^{\text{rel,t}}_{is}$, is computed as:

$$\boldsymbol{v}^{\text{rel,t}}_{is} = \boldsymbol{v}^{\text{rel}}_{is} - (\boldsymbol{v}^{\text{rel}}_{is} \circ \boldsymbol{n}_s). \tag{9}$$

3.2. Heat generation and dissipation

The model incorporates two main heat sources and one heat loss. The heat sources are heat generated by plasticity $\dot{q}^{pl}_i$ and heat generated by friction $\dot{q}^{fric}_i$, while the heat loss is dissipated via the die, the container's outer walls and extruded rod by convection to the surrounding, denoted by $\dot{q}^{conv}_i$. The $\dot{q}^{pl}_i$ is calculated as (Li et al., 2021a; Röthlin et al., 2019)

$$\dot{q}^{pl}_i = \alpha\ \dot{\varepsilon}^{pl}_i\ \sigma^y_i, \tag{10}$$

where α is the Taylor–Quinney coefficient and $\dot{\varepsilon}^{pl}_i$ is the plastic strain rate. The other heat source $\dot{q}^{fric}_i$ is given by (Li et al., 2021a; Röthlin et al., 2019)

$$\dot{q}^{fric}_i = \left\|\boldsymbol{f}^{fric}_{is}\right\|\ \left\|\boldsymbol{v}^{rel,t}_{is}\right\|. \tag{11}$$

The heat convected to the surrounding, $\dot{q}^{conv}_i$, is determined as (Afrasiabi et al., 2021)

$$\dot{q}^{conv}_i = h^{conv}_i\ A^{\text{shear}}_i\ (T_{\text{ref}} - T^s_i). \tag{12}$$

where h^{conv}_i is the convection coefficient. T^s_i is the particle temperature exposed to the surrounding environment, T_{ref} is the surrounding reference room temperature.

3.3. PID controller integration

A PID controller is integrated with the SPH solver to maintain a constant extrusion force throughout the simulation, closely mimicking the experimental FE process. The PID controller dynamically adjusts the die plunging velocity to achieve the desired target force. At each PID sampling time, the current simulation extrusion force is calculated and passed to the PID controller, which calculates the error and applies proportional, integral, and derivative actions to minimize the deviation from the target force over time by updating the die plunging velocity, Fig. 3. The die plunging velocity is given by

$$V_{\text{d}}(t) = \text{sat}\Bigg(\underbrace{K_p\, e(t)}_{\text{Proportional}} + \underbrace{K_i\, I(t)}_{\text{Integral}} + \underbrace{K_d\,\frac{e(t) - e(t-\Delta t_{\text{pid}})}{\Delta t_{\text{pid}}}}_{\text{Derivative}},\ V_{\min},\ V_{\max}\Bigg), \tag{13}$$

where K_p, K_i, and K_d are the proportional, integral, and derivative PID controller gains, respectively. Δt_{pid} is the PID sampling time. $V_{\min}$ and $V_{\max}$ represent the lower and upper limits for the die plunging velocity, respectively, to prevent unphysical extreme displacement. $e(t)$ is the force error at time t and it is given by

$$e(t) = F_{\text{target}} - F_{\text{sim}}. \tag{14}$$

F_{target} is the target constant force during extrusion. F_{sim} is the calculated extrusion force in the simulation, and it is given by

$$F_{\text{sim}} = \sum_{i=1}^{N_c} f^{\text{con}}_{is,z} + f^{\text{fric}}_{is,z}, \tag{15}$$

where N_c is the number of billet particles in contact with the die. $f^{\text{con}}_{is,z}$ and $f^{\text{fric}}_{is,z}$ are the contact and frictional forces in the z direction calculated from Eqs. (1) and (7), respectively. The integral of error is given by

$$I(t) = \text{sat}\Big(I(t - \Delta t_{\text{pid}}) + e(t)\Delta t_{\text{pid}},\ -I_{\max},\ I_{\max}\Big). \tag{16}$$

The integral of error $I(t)$ is implemented with anti-windup clamping range $[I_{\max}, I_{\max}]$ to prevent excessive accumulation that could lead to instabilities. This closed-loop implementation enables reliable force regulation within the SPH simulation, ensuring that the modeled process closely follows the intended operational conditions of the force-controlled FE experiment. Further details on the integration of the PID controller with the SPH solver are summarized in the flowchart presented in Appendix B.

3.4. Model setup

The FE model consists of three main parts: a deformable billet, a rigid container, and a rigid die. The model's geometry is based on the experimental setup in Section 2, while the dimensions, number of particles, and materials are detailed in Fig. 4. The initial spacing between all SPH particles is set to 1 mm, which is selected to balance model prediction accuracy with simulation run time. The heating phase was excluded from the simulation because the die advances only about 0.6 mm during this phase. Accurately modeling such a small movement would require drastically reducing the particle size, which is computationally not feasible. The container's rotational speed of 90 rpm is used as input for the simulation for rotating the die while the container remains fixed. This setup reduces numerical errors that would otherwise arise from rotating the container with the deformable body, i.e., the billet. This adjustment does not compromise the simulation's ability to replicate the experiment, since the interaction between the die and billet depends on their relative velocity, Eqs. (4) and (7), which remains unchanged.

Heat dissipation to the surroundings is modeled by convection across the outer surfaces. To replicate the heat loss to the extrusion machine, i.e., conduction, a higher heat convection coefficient is applied to the outer surface of the die and the bottom surface of the container, following the approach by Zou et al. (2022). In the simulation, a velocity scaling factor of 10 (Elbossily et al., 2025) and a mass scaling factor of 1.0×10^5 are employed. The mass scaling does not compromise accuracy, as the kinetic energy remains below 1.4% of the total internal energy, see C.22. With the current setup, simulating 120 seconds of the friction extrusion process requires approximately 5 hours on a single NVIDIA A100 GPU. Detailed material properties and numerical constants are provided in Appendix E.

4. PID controller response analysis

A total of 27 simulations were performed using different combinations of PID controller gains K_p, K_i, and K_d. Controller performance was assessed using the settling time, defined as the time required for the extrusion force error in the simulation to reach steady state, i.e., remain within ±15% of the 300 kN target value. The mean extrusion force error was calculated to quantify the average deviation of the extrusion force

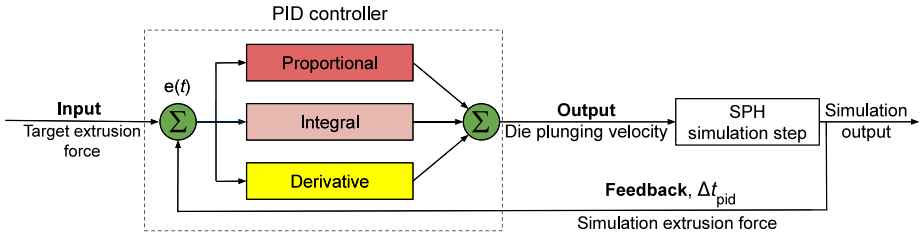

Fig. 3. Schematic representation of the force-based PID control loop integrated within the SPH solver, illustrating the dynamic adjustment of die plunging velocity to maintain the target extrusion force during the simulation.

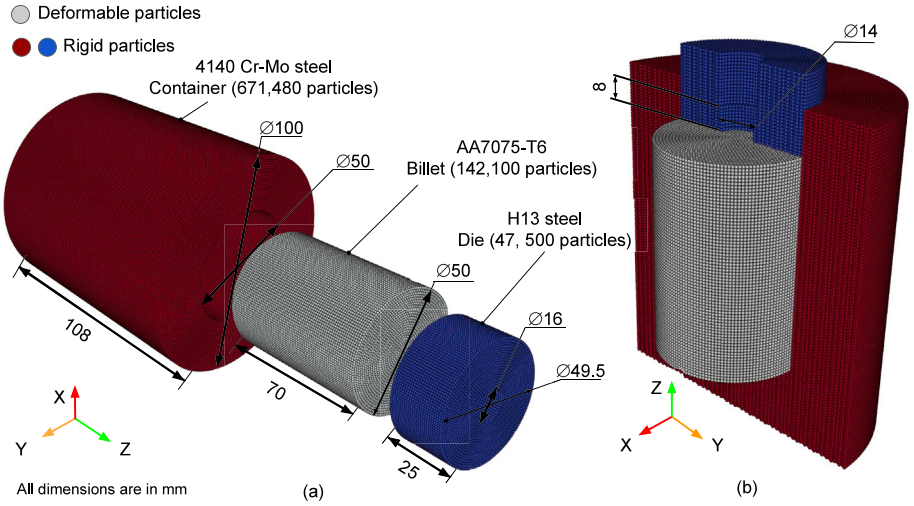

Fig. 4. Proposed model of FE process used in this study: (a) model parts with geometries, dimensions, number of particles, and materials; and (b) assembled model with a cross-section in the container and die. All dimensions are in mm.

from its target. To avoid selecting gains that achieve accurate force tracking through unrealistic die plunging behavior, the maximum and minimum die plunging velocities during the extrusion were recorded. In addition, the coefficient of variance of the die plunging velocity was computed to quantify deviations from their respective mean values and capture fluctuation levels. The PID controller gains and their corresponding performance metrics are summarized in Table D.1.

To identify the optimal PID controller gains, a Pareto plot was used to visualize the trade-off between extrusion force settling time, mean steady-state error, and the coefficient of variation of die plunging velocity. Simulated sets with settling times over 60 seconds were excluded, as they were considered not to reach steady state. Fig. 5 displays the five remaining sets. Among them, Set 2 lies on the Pareto frontier, offering a favorable balance of a good settling, low error, and a smooth velocity profile. It was therefore selected for validating the proposed model. It is noted that the reported settling times are comparatively large because the heating and ramping phases were omitted in the simulation, requiring additional time for the billet to be heated up.

Fig. 6 shows the simulated extrusion force and the individual contributions of the proportional, integral, and derivative terms to the PID controller output—the die plunging velocity for Set 2. The proportional and integral terms dominate the controller's response, while the derivative term has only a minor influence. Increasing the derivative gain, as in Sets 5 and 6 in Table D.1, increases the settling time and makes the simulation harder to reach the steady state, along with a higher die plunging velocity fluctuation. This observation is consistent with process physics: as the billet heats up from friction and deformation, the material's flow stress decreases gradually. Because this softening occurs smoothly, force errors naturally diminish over time, and the controller rarely needs to counteract abrupt changes.

5. Model validations

The model is validated via experimental measurements for the extrusion force, die plunging displacement, and the temperature of the thermocouple in the die, Fig. 7. Both the experiments and the simulations are conducted under force-controlled conditions, and the validation focuses on comparing the resulting process responses rather than the internal PID controller parameters, which are inherently machine-specific. Despite the initial omission of 36 seconds of the heating and ramping phases in the simulation, the predicted extrusion force stabilized at approximately 300 kN, closely matching the experimental result with an RMSE of 8.6 kN during steady state. The simulated die displacement also exhibits a strong correspondence with the experimental measurements, both in absolute value and in slope, demonstrating the capability of the model to reproduce the die movement observed based on a force-control setup. Regarding the die temperature, it starts with an initial deviation from the experimental measurement due to omitting the heating phase; however, this discrepancy progressively diminished as the simulation advanced. The comparison demonstrates strong agreement between the simulation and the experimental temperatures, indicating the model's ability to accurately capture thermal and mechanical responses during extrusion.

In addition to validating the die temperature, the simulation-predicted billet temperature was explicitly compared against the experimental measurements from 12 thermocouples embedded in the billet within three same experiments, showing excellent

[1] Die plunging displacement during the first 32 seconds was excluded from the simulation because of omitting the heating and ramping phases, and it is plotted on the negative side of the Y axis.

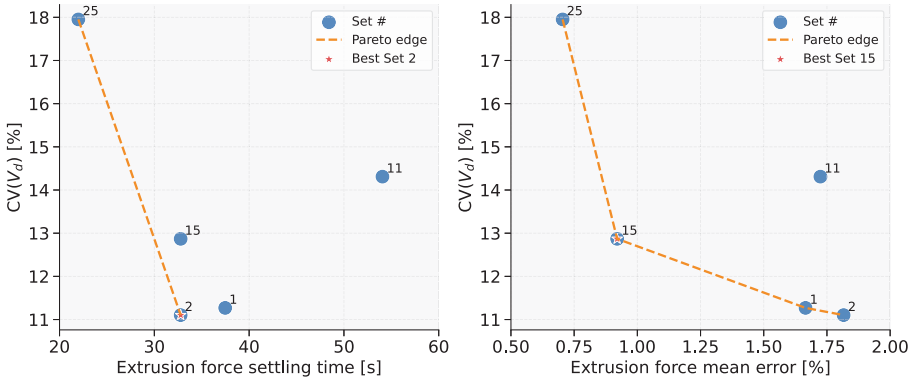

Fig. 5. Pareto plot showing the trade-off between the extrusion force settling time and the extrusion force mean error VS. the coefficient of variation of the die plunging velocity, CV(V_d).

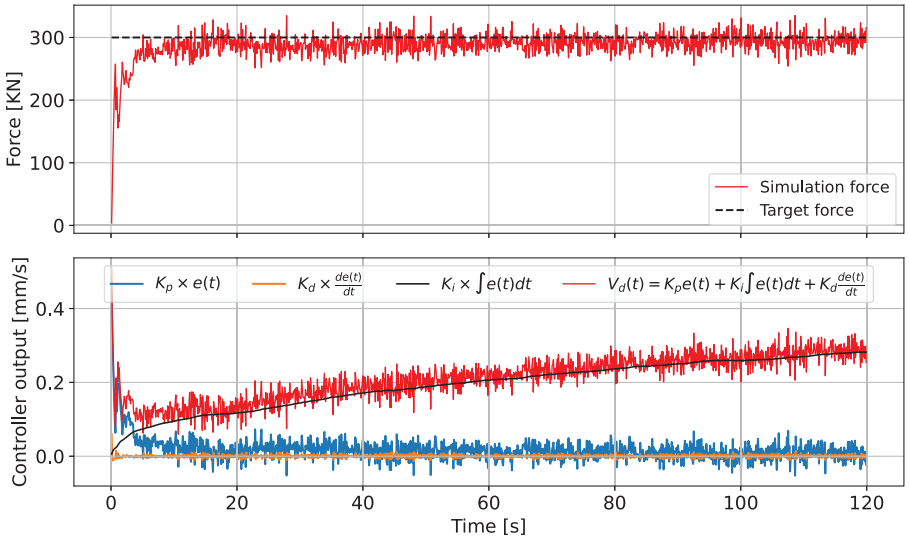

Fig. 6. Simulation extrusion force and PID controller output for Set 2, showing the proportional, integral, and derivative contributions to the die plunging velocity. The proportional and integral terms dominate, while the derivative term has minimal influence.

agreement, Fig. 8. The spatial temperature distribution of the billet during extrusion was obtained by interpolating the measured thermocouple data, see Fig. 9. The experimental and numerical distributions show close agreement and indicate that the billet is continuously heated during extrusion, with a temperature gradient increasing toward the die–billet contact surface.

To provide a complete view of heat generation and dissipation during extrusion, Fig. 10 shows the temperature distribution across the billet and the central cross-section of the container and die at various time steps in the simulation. Furthermore, the relative contributions of heat from friction and plastic deformation are illustrated in Fig. 10e. The primary heat source is plastic deformation, driven by the sticking of the billet's top surface against the die. This is confirmed by tracking the tangential velocity of the billet material in contact with the die during steady state, which closely matches the velocity of the die surface, as shown in Fig. 11. As the material softens, the frictional force eventually exceeds the maximum shear force the material can withstand. As a result, the material in contact with the die is sheared and stuck to the die surface. A stick–slip condition is observed near the container walls, where interactions between the particles and the container walls slow down particles' motion, causing them to slip relative to the die. Heat dissipates from the container, die, and extruded rod to the surroundings through convection. A temperature gradient develops from the die-billet interface toward the billet bottom because most plastic deformation, i.e., the highest heat generation, occurs at the billet's top surface. In addition, since the container bottom is connected to the machine, it conducts more heat away compared to the container walls, which are exposed only to limited free convection.

6. Material flow and plastic strain evaluation

Tracking the deformation of the twelve thermocouples inside the billet using micro-computed tomography after extrusion shows that material near the orifice follows a straight path directed toward the orifice. This path deforms as the material's radial distance from the orifice increases, Fig. 12. This deformation is attributed to increasing tangential velocity away from the orifice as an indication of material sticking to the die, which is confirmed by analyzing the tangential velocity of the billet and die predicted in the simulation, Fig. 11.

To capture the material flow from the die to the extruded rod, four particles—P1, P2, P3, and P4—were tracked within the billet in the simulation. They were initially positioned at radial distances of 6, 9, 12, and 16 mm, respectively, and 10 mm below the billet's top surface, Fig. 13a. Particles closer to the billet center, P1 and P2, follow a relatively short helical path and are extruded closer to the center of the rod. In contrast, particles positioned nearer to the billet's outer surface, P3 and P4, exhibit a longer helical path and end up closer to the rod's periphery, Fig. 13b. The length of the particle path before extrusion

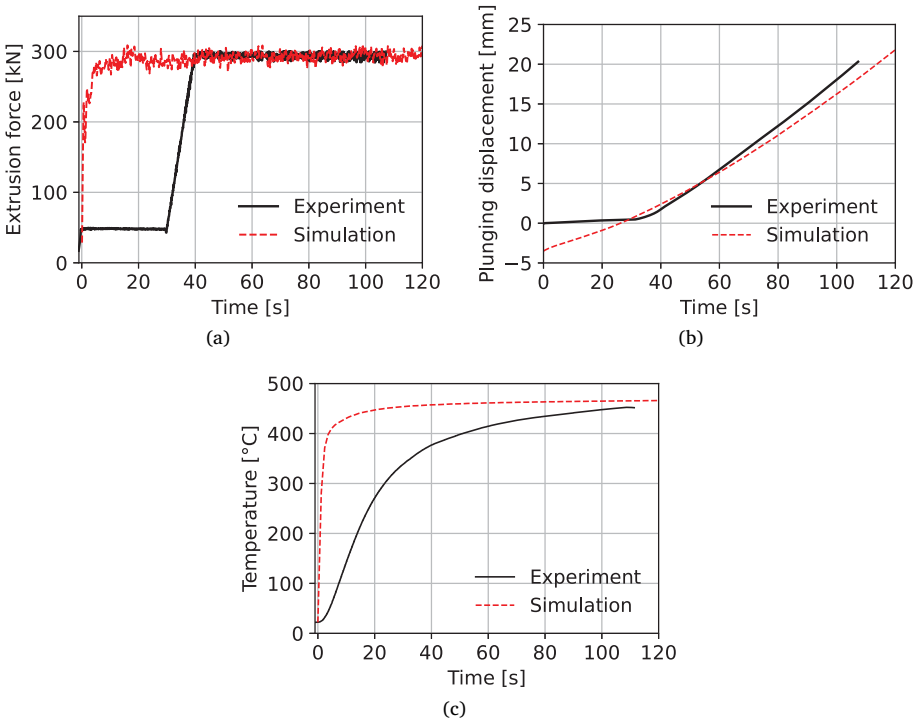

Fig. 7. Model validations: (a) extrusion force; (b) die plunging displacement[1]; and (c) die temperature.

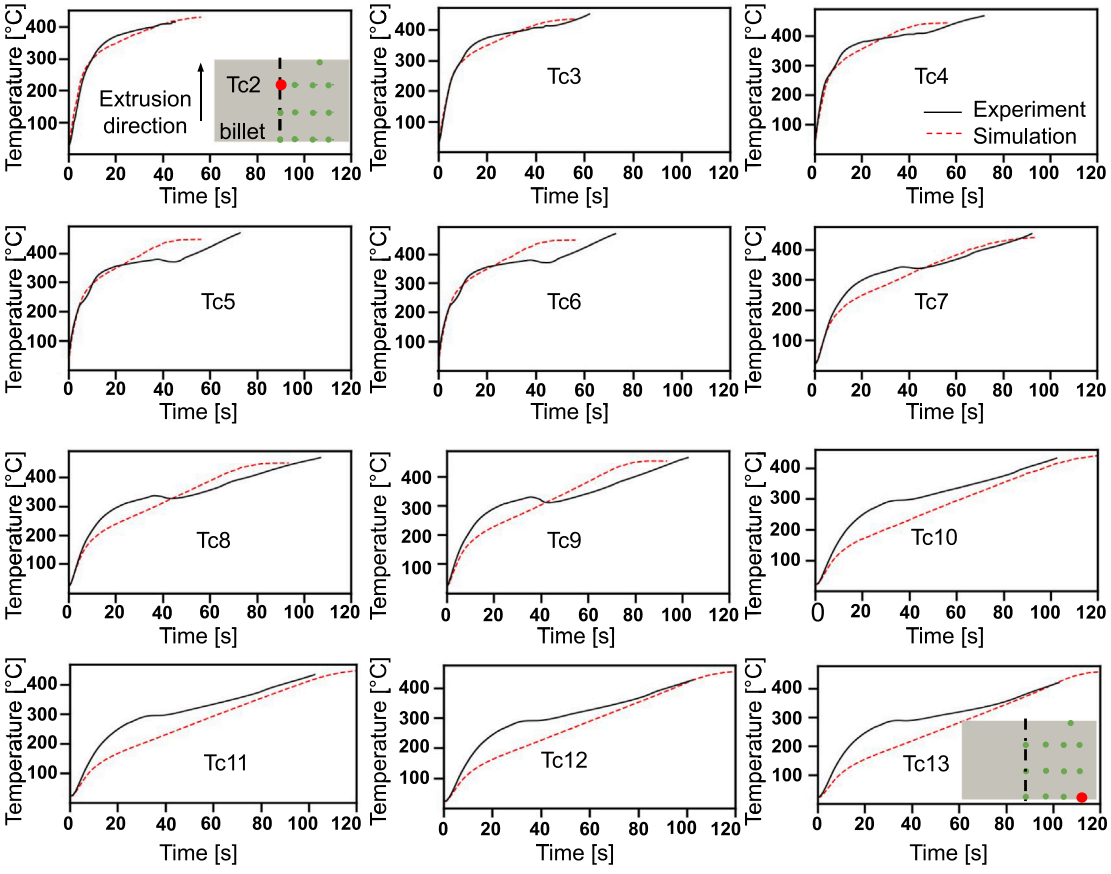

Fig. 8. Comparison of simulation and experiment for process temperature evolution during friction extrusion at twelve positions within the billet material.

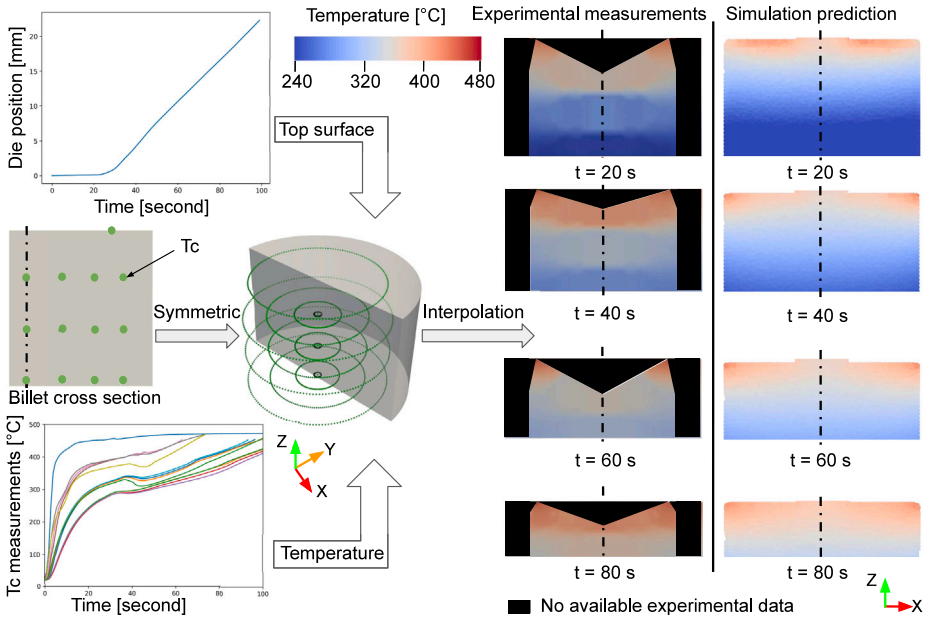

Fig. 9. Schematic illustration of the interpolation of measured billet temperatures VS. simulation predictions at various time steps.

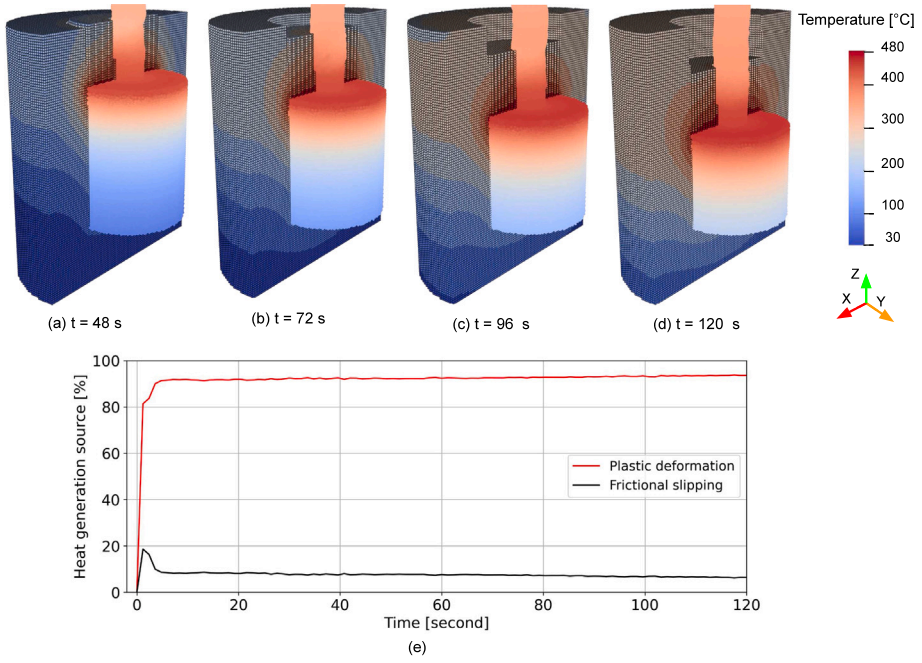

Fig. 10. (a)–(e) Predicted temperature distributions for the billet and a central cross-section of the container and die at different time steps. (e) Predicted heat generation source from friction and plastic deformation during the simulation.

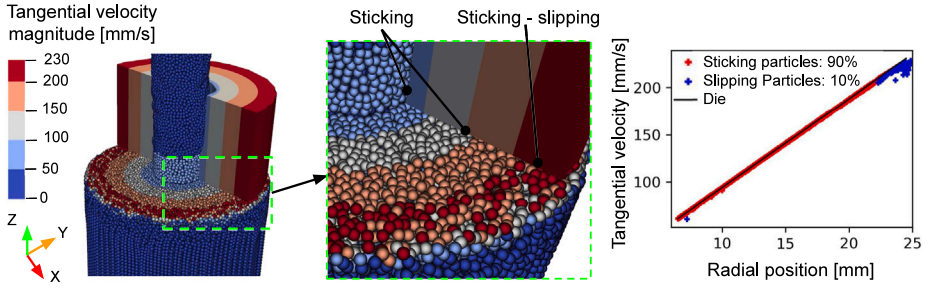

Fig. 11. Tangential velocity field of the billet material and die during FE at $t = 80$ s, highlighting the sticking–slipping percentage of the particle in contact with the die.

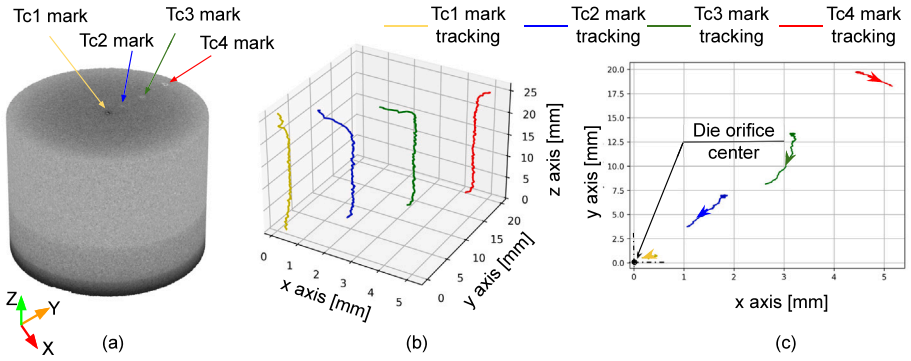

Fig. 12. Deformation paths of thermocouples post-extrusion: (a) CT scanned billet; (b) 3D visualization of extracted thermocouple deformation paths; and (c) 2D projection of the deformed paths, illustrating curvature away from the orifice due to tangential material flow.

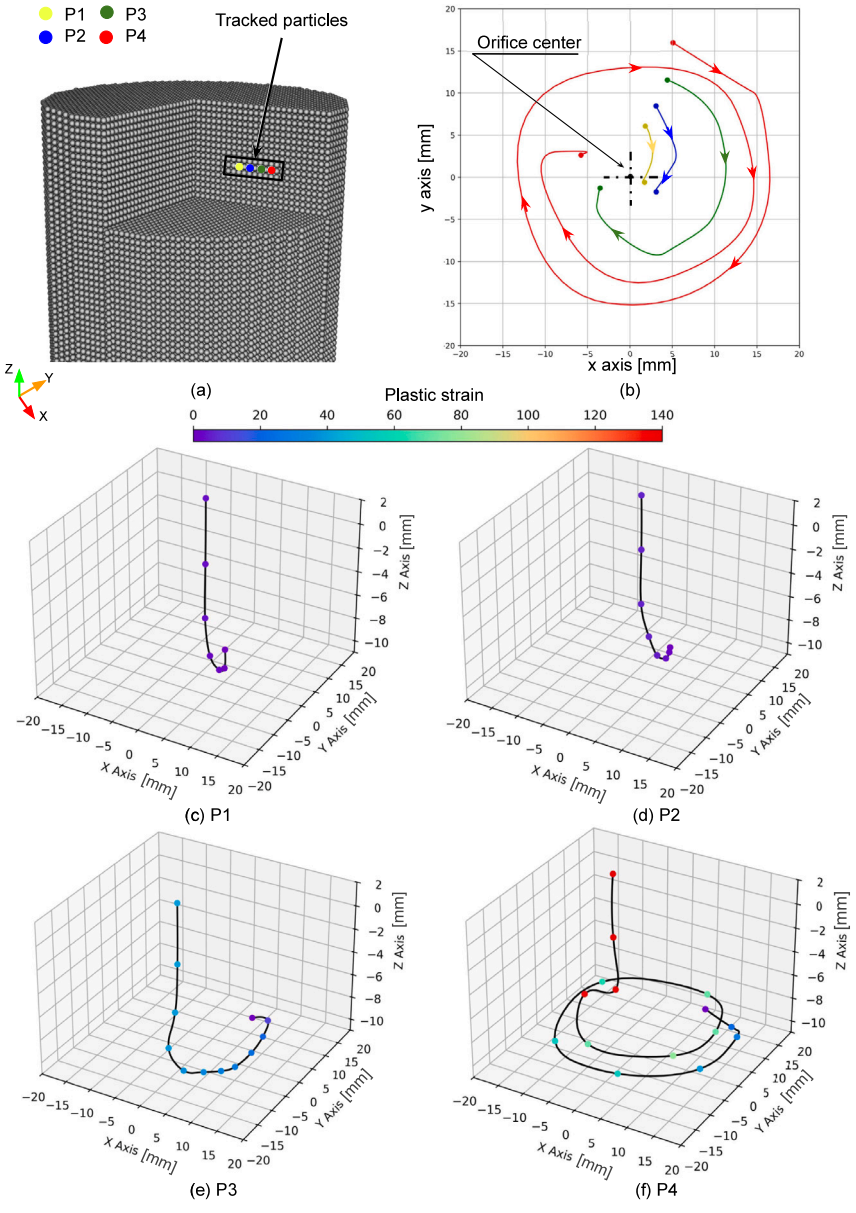

Fig. 13. Position tracking for a set of particles, P1, P2, P3 and P4: (a) initial positions of tracked particles within the billet; (b) 2D position tracking of the particles, showing the variation in their paths based on their initial positions; and (c)–(f) 3D position tracking and evolution of plastic strain for the four tracked particles, highlighting the increase in the plastic deformation from P1 to P4.

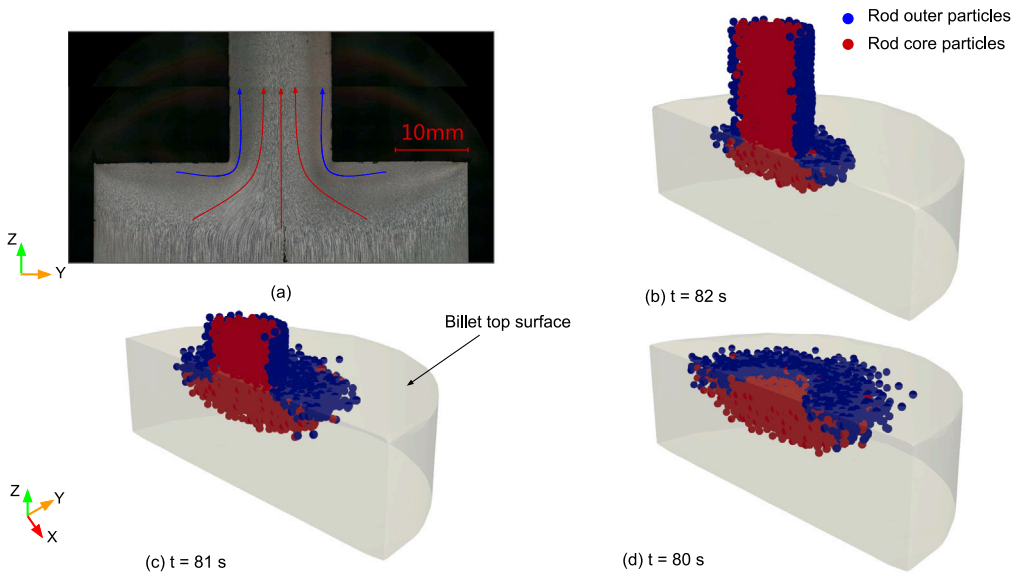

Fig. 14. (a) Microscopic cross-section of the billet and extruded rod at the end of the experiment. (b) Tracked extruded rod outer particles with radial positions greater than 12 mm, highlighted in blue. (c) and (d) Backtracking of the outer particles confirms their origin from the billet top surface beneath the die.

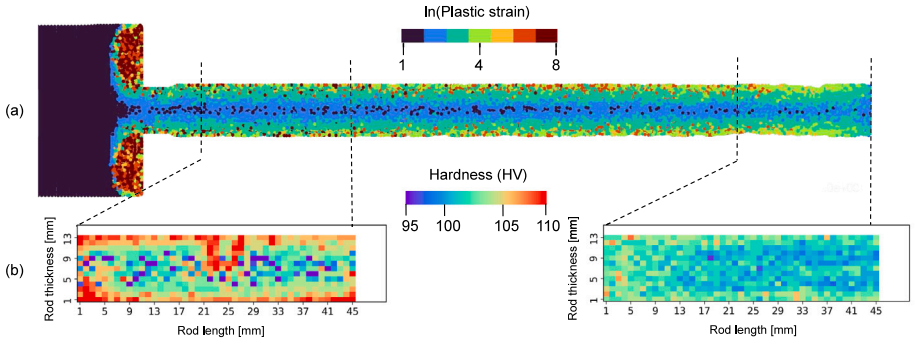

Fig. 15. (a) Simulation-predicted plastic strain for the cross-sectional view of the billet and extruded rod. (b) Experimental hardness measurements of the extruded rod at corresponding locations.

influences the degree of plastic deformation experienced—the longer the path, the higher the plastic deformation. This trend is evident in the tracked particles, with P1 experiencing the least plastic strain and P4 the most, Figs. 13(c–f).

A cross-sectional microscopic analysis of the billet and the extruded rod at the end of the experiment suggests that the rod's outer surface consists of fine grains primarily formed from the billet material located directly beneath the die. In this region, the material is subjected to high strain rates and elevated temperatures, leading to the formation of finer grains. In contrast, the core of the rod consists of larger elongated grains, mainly extruded from the core of the base material, as shown in Fig. 14a. This observation is supported by tracking the position of the extruded rod particles with a final radial position greater than 12 mm, highlighted in Fig. 14b. Fig. 14c and 14d present the particle backtracking positions, confirming that the extruded rod outer particles originate mainly from the billet top surface. Material flow pattern results in higher plastic strain on the extruded rod's outer surface compared to its core, as the billet material under the die, from which the outer surface of the rod is formed, is subjected to the highest plastic strain as predicted by the simulation, Fig. 15a. In contrast, the rod tip shows lower plastic strain since the material there undergoes less deformation path to be extruded. The predicted plastic strain distribution of the rod aligns with hardness measurements of the rod's cross-section, Fig. 15b, which show increased hardness at the outer surface compared to the core as well as reduced hardness at the rod tip compared to the remaining extruded rod.

7. Microstructure regions and grain size analysis

In the FE process, the billet material is subjected to high temperatures and strain rates, resulting in thermomechanical conditions under which dynamic recrystallization (DRX) (Huang and Logé, 2016) is expected to occur, leading to grain refinement as observed experimentally. The grain size is not directly predicted by the present simulations, as no explicit DRX kinetics or grain size evolution model is implemented. Instead, the Zener–Hollomon parameter is evaluated and used to infer relative trends in grain refinement based on established experimental correlations. The Zener–Hollomon parameter, $Z = \dot{\epsilon} \cdot e^{\frac{Q}{RT}}$ (Lin et al., 2023), is used to quantify the combined influence of mechanical (strain rate $\dot{\epsilon}$) and temperature (T) effects on grain size. Here, Q is the material's activation energy, set at 150 kJ/mol, and R represents the universal gas constant, 8.314 J/mol K (Trimble and O'Donnell, 2015). Higher strain rates and lower temperatures lead to increased Z values, indicating grain refinement. Notably, the strain rate rises toward the container wall as the material sticks to the die and tangential velocity increases, while the highest temperature occurs on the billet's top surface due to the high plastic deformation, Fig. 16a. This combination yields a Z distribution that the thermo-mechanically affected zone (TMAZ) and the base material (BM) observed experimentally, Fig. 16b.

Microstructure analysis of the extruded rod after die advances of 10, 20, and 30 mm shows progressive grain refinement for the extruded rod, Fig. 17. This refinement is consistent with the increased strain

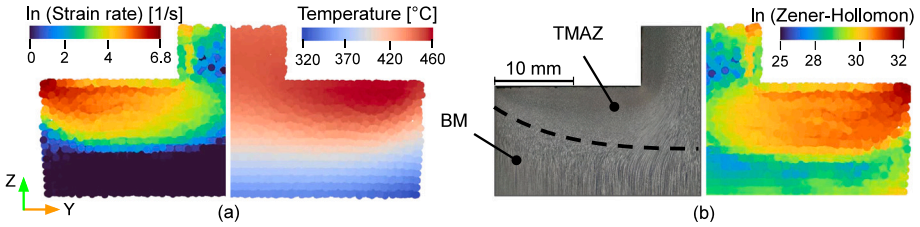

Fig. 16. (a) Predicted strain rate and temperature distribution at the end of the extrusion process in the simulation. (b) Zener–Hollomon value with the experimental identifications of microstructural zones, including TMAZ and BM.

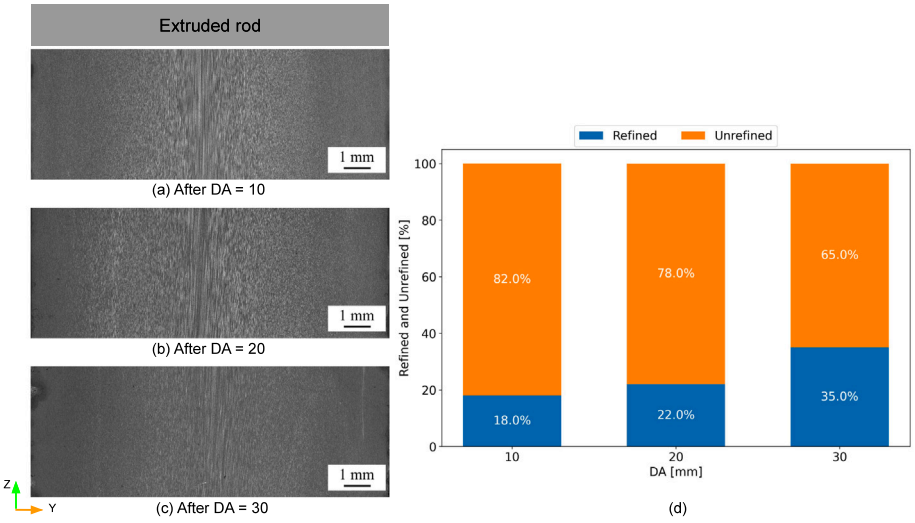

Fig. 17. Etched macrographs of the extruded rod after 10 mm (a), 20 mm (b), and 30 mm (c) die advancement (DA), showing larger and elongated grains in the center and refined grains at the outer radius. As the DA increases, the grains in the extruded rod are progressively refined (d).

rate in the extrusion direction for the billet core immediately before extrusion, Fig. 18. Throughout the extrusion, the die–billet interface temperature remains stable within the DRX temperature range for AA7075 (350–450 °C) (Ye et al., 2024; Zhu et al., 2007), see Figs. 9 and 10. Meanwhile, the average billet temperature rises, reducing the flow stress of the material. This softening triggers the PID controller to increase the die plunging speed to maintain a constant extrusion force, thereby further elevating the strain rate in the extrusion direction for the central region. The elevated strain rate in the extrusion direction increases the Zener–Hollomon parameter, which suggests a tendency toward finer recrystallized grains along the extruded rod length, whereas the strain rate in the traverse direction remains largely unchanged and plays a secondary role in microstructural refinement.

The simulation was repeated with a constant die and container outer surface temperature of 22 °C to mimic the effect of an external cooling system. Imposing cooling on the external surfaces of the die and container stabilizes the die plunging velocity and, consequently, maintains a constant strain rate in the extrusion direction, Fig. 19. This stability is critical for grain-size uniformity along the rod length, as increases in the strain rate in the extrusion direction directly influence DRX kinetics and, therefore, change grain size along the extruded length. Moreover, the external temperature cooling reduces the die–billet interface temperature as well as the temperature of the material about to be extruded, further enhancing DRX. This improvement is evidenced by higher steady-state Zener–Hollomon values, Fig. 20c. Furthermore, decreasing the temperature of the extruded rod increases its material's flow stress, resulting in a more uniform plastic strain along the rod's core, Fig. 20d. Therefore, the development of an experimental cooling system for the friction extrusion systems represents one of the next steps in the further development of the setup.

8. Conclusion

This work introduced the first GPU-accelerated meshfree framework that couples smoothed particle hydrodynamics with a PID controller to model the force-controlled friction extrusion of 14 mm rods from AA7075-T6 billets. By combining high-fidelity simulations with detailed experimental validation, including full-field thermal measurements and post-process microstructural characterization, the study bridges a critical gap in predictive modeling of the friction extrusion process. The integration of closed-loop control into the numerical model enables, for the first time, direct simulation of the force-controlled process without relying on prescribed die displacement profiles. The results demonstrate that the framework can accurately capture the process thermomechanics and material flow, while GPU acceleration reduces the computation time to under five hours on a single modern GPU, compared to the hundreds of hours previously required, thereby making simulation-based tuning of the PID controller feasible. The combined numerical–experimental investigation reveals the following key findings:

- The die–billet interface temperature remains nearly constant during extrusion, while the billet bulk temperature increases continuously.
- Material near the die orifice follows shorter helical flow paths and undergoes lower plastic deformation compared to material originating from the billet periphery.
- The outer surface of the rod primarily forms from the high-shear zone and exhibits finer grains and larger plastic deformation, whereas the core originates predominantly from the billet base material.

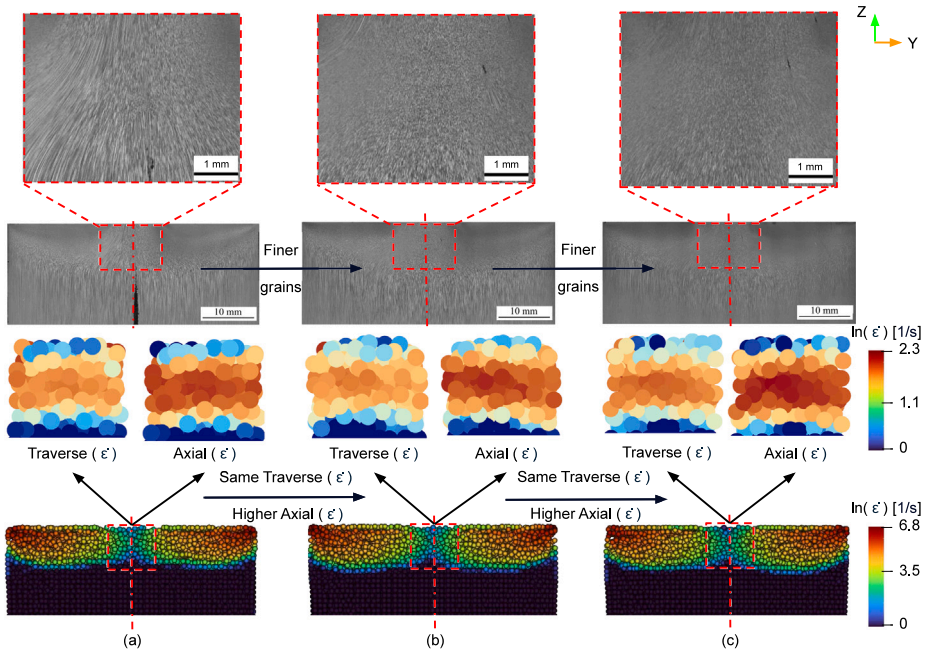

Fig. 18. Macrographs and corresponding strain rate distributions decomposed into two components: (i) axial strain rate in the extrusion direction and (ii) transverse strain rate in the billet cross-section, shown after die advancements of (a) 10 mm, (b) 20 mm, and (c) 30 mm. Results show progressive grain refinement and increasing axial strain rate with die advancement.

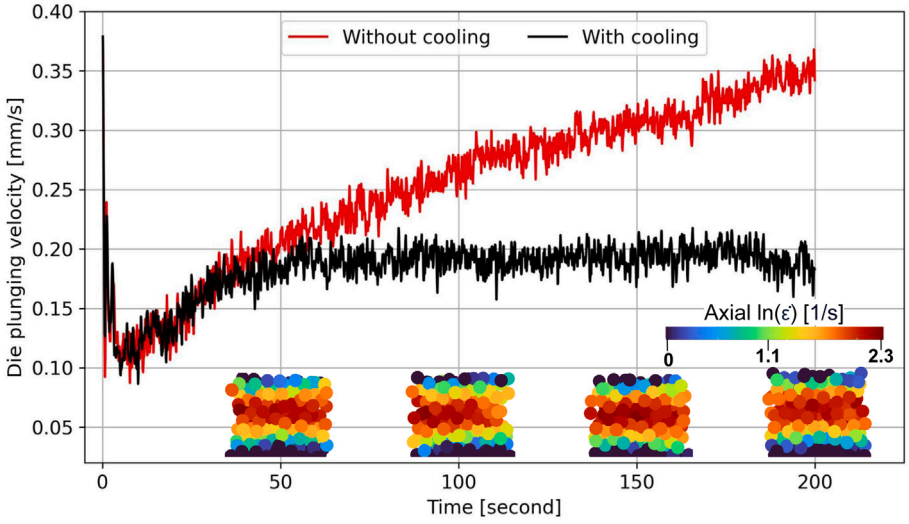

Fig. 19. Stabilizing effect of external cooling on die plunging velocity and axial strain rate in extrusion direction for the billet core under the die orifice before extrusion, illustrated after 50, 100, 150, and 200 seconds of extrusion.

- Grain size along the extruded rod length varies systematically with the increasing strain rate in the extrusion direction, which is primarily governed by the PID controller response compensating for billet softening in order to maintain the prescribed extrusion force.
- The simulation framework suggests that active cooling of the die and container can stabilize strain-rate evolution, promote more uniform grain size along the extrudate, and enhance overall microstructural refinement.

Overall, the presented PID–SPH framework advances the predictive capability of friction extrusion simulations by enabling a physically consistent representation of force-controlled process conditions. It demonstrates both efficiency and accuracy, enabling systematic numerical exploration of process parameters at different force levels and reducing the need for preliminary experimental trials.

CRediT authorship contribution statement

Ahmed Elbossily: Writing – review & editing, Writing – original draft, Visualization, Validation, Software, Methodology, Investigation, Formal analysis, Data curation, Conceptualization. **Zina Kallien:** Writing – review & editing, Visualization, Investigation, Formal analysis, Data curation. **Lars Rath:** Writing – review & editing, Visualization, Validation, Formal analysis, Data curation. **Rupesh Chafle:** Writing – review & editing, Investigation, Data curation. **Mohamadreza Afrasiabi:** Writing – review & editing, Software, Methodology. **Benjamin Klusemann:** Writing – review & editing, Supervision, Project administration, Methodology, Funding acquisition, Conceptualization.

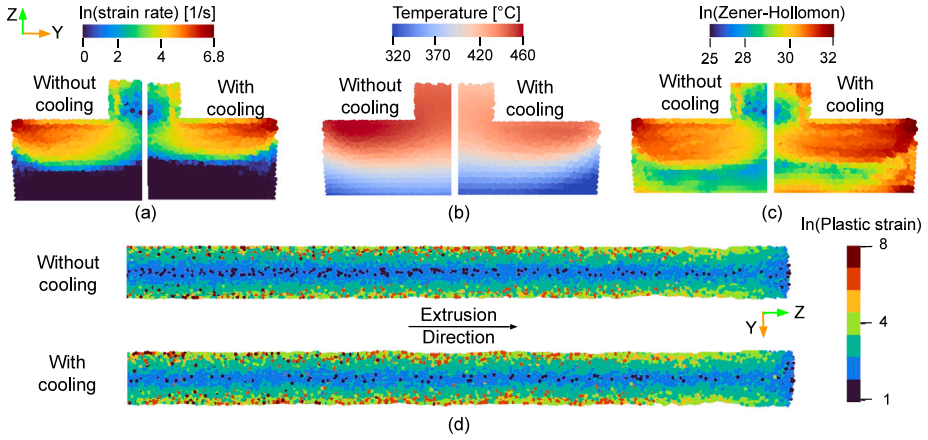

Fig. 20. Comparison of key process parameters with and without external cooling showing: (a) slightly reduced strain rates; (b) reduced temperature profile; (c) higher Zener–Hollomon values; and (d) more uniform core plastic strain in the extruded rod after applying external cooling. This illustrates the potential of external cooling to the friction extrusion process.

Declaration of Generative AI and AI-assisted technologies in the writing process

During the preparation of this work, the authors used ChatGPT in order to identify typos and improve language/readability. After using this tool, the authors reviewed and edited the content as needed and take full responsibility for the content of the publication.

Funding

This project has received funding from the European Research Council (ERC) under the European Union's Horizon 2020 research and innovation program (grant agreement No 101001567).

Declaration of competing interest

The authors declare that they have no known competing financial interests or personal relationships that could have appeared to influence the work reported in this paper.

Appendix A. Notation

The notation used throughout this paper is as follows:

x denotes a scalar and $\boldsymbol{x}$ represents a vector. $\boldsymbol{x}_1 \cdot \boldsymbol{x}_2$ denotes the dot product of two vectors, where $\boldsymbol{x}_1 \circ \boldsymbol{x}_2$ is the Hadamard product and $\boldsymbol{x} \times \boldsymbol{x}$ represents the cross product of two vectors. $\dot{x}$ represents the time derivative of x. The L2-norm of a vector is denoted as $\|\boldsymbol{x}\|$. $\text{sat}(x, a, b) = \min(\max(x, a), b)$ denotes limiting x to the interval $[a, b]$.

Appendix B. PID controller integration with SPH solver

The simulation begins with an initialization stage in which static parameters such as material properties, numerical parameters, and PID controller gains are defined on the CPU and transferred to the GPU. During each time step, the dynamic part of the model is executed entirely on the GPU and involves solving the SPH governing equations for mass continuity, momentum conservation, and heat transfer, followed by time integration of the state variables. Contact forces between the die and the deformable material are evaluated based on the penalty algorithm. At prescribed PID sampling intervals, the force error is computed and used by the PID controller to update the die velocity. The updated die velocity is then applied through the boundary conditions for the subsequent time step. Reporting and data transfer to the CPU are performed at predefined intervals. The overall workflow and the separation between static initialization and dynamic time-stepping are summarized in the flowchart shown in Fig. B.21.

Table D.1
PID controller gain sets and corresponding performance metrics: settling time and mean error of the simulated extrusion force, $\text{ST}(F_{\text{sim}})$ and $\text{ME}(F_{\text{sim}})$; maximum and minimum die plunging velocities, $\text{Max}(V_{\text{d}})$ and $\text{Min}(V_{\text{d}})$; and coefficient of variation of die plunging velocity, $\text{CV}(V_{\text{d}})$.

Set	K_p –	K_i –	K_d –	$\text{ST}(F_{\text{sim}})$ [s]	$\text{ME}(F_{\text{sim}})$ [%]	$\text{Max}(V_{\text{d}})$ [mm/s]	$\text{Min}(V_{\text{d}})$ [mm/s]	$\text{CV}(V_{\text{d}})$ [%]
1	0.015	0.02	1e−5	37.474	1.665	0.400	0.217	11.270
2	0.015	0.02	2e−5	32.777	1.816	0.336	0.159	11.103
3	0.015	0.02	4e−5	107.626	2.115	0.346	0.165	11.997
4	0.015	0.04	1e−5	94.035	1.993	0.356	0.142	14.618
5	0.015	0.04	2e−5	111.523	0.949	0.353	0.180	11.241
6	0.015	0.04	4e−5	86.840	0.884	0.342	0.172	12.196
7	0.015	0.06	1e−5	76.048	0.983	0.365	0.159	13.355
8	0.015	0.06	2e−5	104.728	0.547	0.370	0.183	10.391
9	0.015	0.06	4e−5	112.623	0.611	0.391	0.177	12.324
10	0.020	0.02	1e−5	80.445	0.481	0.369	0.151	13.152
11	0.020	0.02	2e−5	54.063	1.724	0.345	0.134	14.310
12	0.020	0.02	4e−5	64.256	1.836	0.351	0.141	14.489
13	0.020	0.04	1e−5	66.254	1.884	0.368	0.123	16.588
14	0.020	0.04	2e−5	69.752	0.729	0.369	0.160	13.630
15	0.020	0.04	4e−5	32.777	0.920	0.367	0.171	12.869
16	0.020	0.06	1e−5	99.532	0.896	0.393	0.083	15.627
17	0.020	0.06	2e−5	100.131	0.678	0.368	0.131	13.945
18	0.020	0.06	4e−5	119.718	0.680	0.400	0.158	15.323
19	0.025	0.02	1e−5	116.220	0.552	0.400	0.118	15.506
20	0.025	0.02	2e−5	73.649	1.773	0.352	0.096	16.338
21	0.025	0.02	4e−5	92.536	1.985	0.400	0.110	20.357
‘ 22	0.025	0.04	1e−5	106.727	1.939	0.400	0.102	18.184
23	0.025	0.04	2e−5	83.043	0.868	0.386	0.146	15.939
24	0.025	0.04	4e−5	109.625	0.822	0.383	0.100	17.200
25	0.025	0.06	1e−5	21.985	0.704	0.400	0.125	17.951
26	0.025	0.06	2e−5	69.152	0.491	0.385	0.115	16.248
27	0.025	0.06	4e−5	67.254	0.618	0.393	0.153	16.670

Appendix C. Energy evolution during simulation

Fig. C.22 illustrates the histories of kinetic energy, internal energy, and their ratio for the billet particles, showing that the kinetic energy remains lower than 1.4%.

Appendix D. PID controller tuning

Table D.1 presents the different PID controller gain sets employed in the simulations together with their corresponding performance metrics for tuning the PID controller gains.

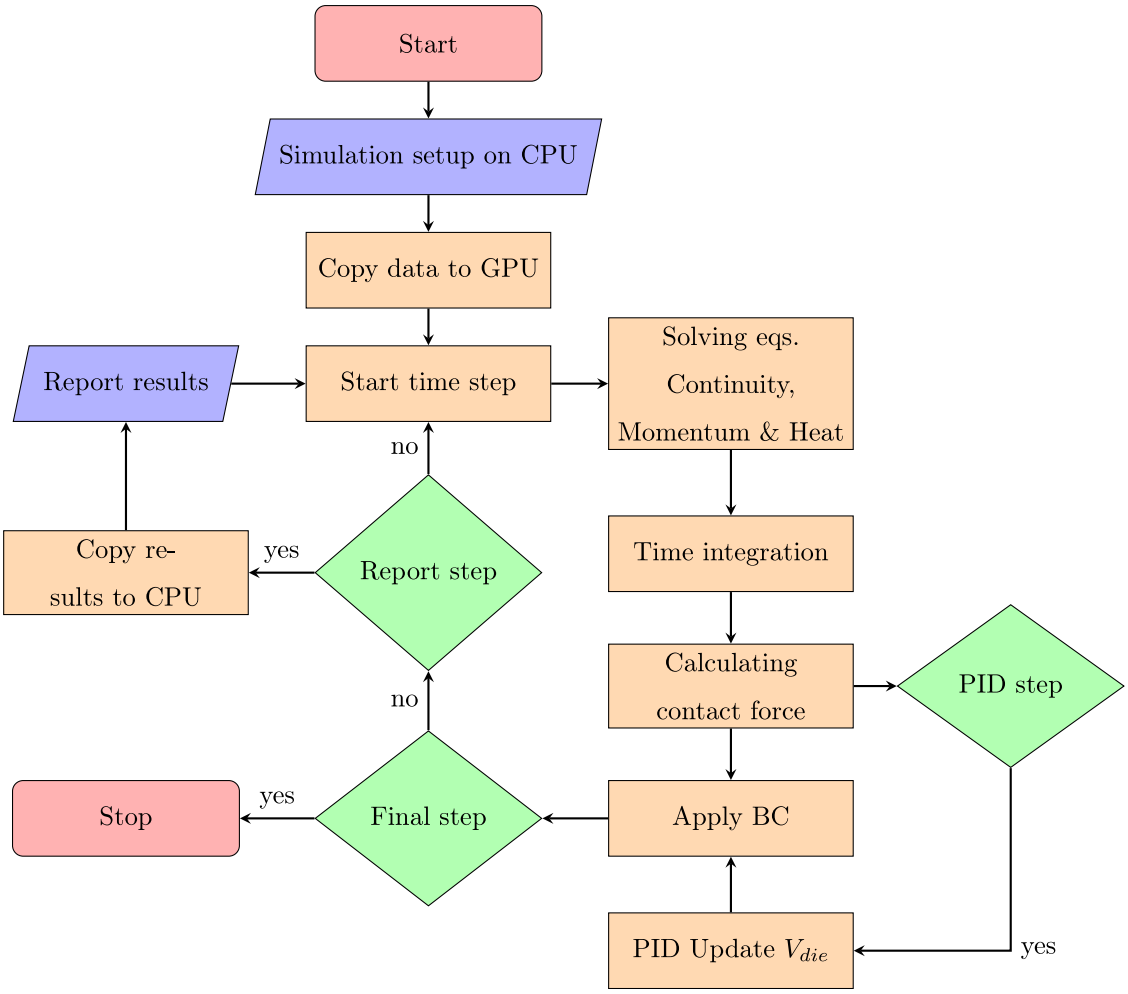

Fig. B.21. Flowchart of the PID-SPH model logic at each time-step.

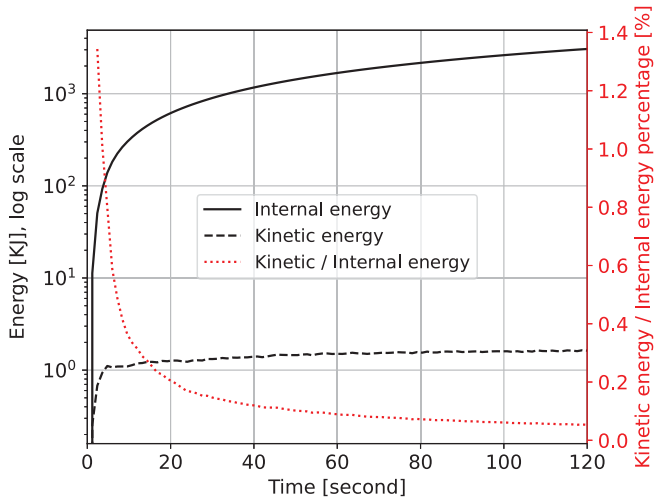

Fig. C.22. Time histories of kinetic energy, internal energy, and their ratio for the billet during simulation. Since the kinetic/internal energy ratio is comparably small, the mass scale is assumed to be not influencing the results.

Table E.2
Material properties of AA7075-T6 (Ma et al., 2020), H13 and AISI 4140 steel (MatWeb, 2025).

Parameters	Symbols	AA7075-T6	H13	AISI 4140	Unit
Density	ρ	2810	7800	7850	kg/m^3
Poison's ratio	ν	0.33	0.3	0.29	–
Elastic modulus	E	71.7	210	205	GPa
Thermal conductivity	$K(T)$	$166.1 - 50.1[\frac{T-T_0}{T_m-T_0}]$	24	42.6	W/mK
Heat capacity	$c_p(T)$	$795.8 - 350.4[\frac{T-T_0}{T_m-T_0}]$	460	519	J/K

Table E.3
JC material parameters of the billet: AA7075-T6 (Brar et al., 2009). No strain hardening has been assumed, i.e., B = 0 MPa.

A [MPa]	C [–]	m [–]	T_0 [°C]	T_m [°C]	$\dot{\varepsilon}_0$ [1/s]
546.0	0.024	1.57	22	477	1.0

Appendix E. Material properties and simulation constants

The employed material properties and the JC material parameters for AA7075-T6 used in this study are presented in Tables E.2–E.3. At the elevated temperatures and high strain levels typical of FE processing, the mechanical behavior of AA7075-T6 is largely governed by DRX (Suhuddin et al., 2023). DRX facilitates the formation of new, strain-free grains that replace the deformed microstructure, leading to a reduction in flow stress. This softening effect compensates the stress

Table E.4
Simulation parameters employed in the SPH simulation of the FE process.

Parameters	Symbols	Values	Reference	Equation
Penalty factor	P	0.1	Stubblefield et al. (2021)	(3)
Damping factor	D	0.2	Stubblefield et al. (2021)	(3)
Coefficient of friction	μ	0.6	Li et al. (2022)	(7)
Taylor–Quinney coefficient	α	0.9	Li et al. (2022)	(10)
Heat convection coefficient [W/m^2°C]	h_i^{conv}	25, 1000[a]	Zou et al. (2022)	(12)
PID Sampling time [s]	Δt_{pid}	0.01	–	(13)
PID die velocity limits [mm/s]	$V_{\min}$, $V_{\max}$	−0.04, 0.4	–	(13)
PID Integral anti-windup limits [mm/s]	$I_{\max}$, $I_{\min}$	−0.01, 0.4	–	(16)

[a] A heat convection coefficient of $h_i^{conv} = 1000$ [W/m^2°C] is employed on the outer surface of the die and the bottom surface of the container, while $h_i^{conv} = 25$ [W/m^2°C] is used for all other outer surfaces of the model.

increase from strain hardening, resulting in stress–strain responses that closely approximate ideal plasticity at high temperatures (Lin et al., 2020). Following the approach of Li et al. (2021a), strain hardening is therefore neglected in the subsequent analysis, and ideal plasticity is assumed. A friction coefficient of 0.6 was adopted in the simulations based on the work of Li et al. (2022), who used the same value in their SPH modeling of friction extrusion of AA7075 tubes. A variation of the friction coefficient by ±20% was found to have a small influence on the temperature evolution. As the process progresses, the material softens due to increasing temperature, leading to a reduction in its allowable shear strength. Under these conditions, sticking at the die-billet interface is readily established for friction coefficient values within the ±20% range around the reference value. Consequently, plastic deformation remains the dominant heat generation mechanism, and small variations in frictional heating do not lead to a significant effect on the overall temperature response.

Additional constants applied in the simulation are listed in Table E.4.

Data availability

The solver is released as open-source code via GitHub (https://github.com/SPH-SSMP/FE-SPH-GPU) and the experimental data and simulation results are available at Zenodo (https://doi.org/10.5281/zenodo.18657543).

References

Afrasiabi, M., Klippel, H., Roethlin, M., Wegener, K., 2021. An improved thermal model for SPH metal cutting simulations on GPU. Appl. Math. Model. 100, 728–750. http://dx.doi.org/10.1016/j.apm.2021.08.010.

Akar, S., Kinchin, C., Kurup, P., 2022. Techno-Economic Analysis for Shear Assisted Processing and Extrusion (ShAPE) of High Strength Aluminum Alloys. Technical Report, National Renewable Energy Lab. (NREL), Golden, CO (United States), http://dx.doi.org/10.2172/1846614.

Aspes, P., Kallien, Z., Rath, L., Suhuddin, U., Klusemann, B., 2025. Effect of consumable stud microstructure on friction surfacing: Comparison between friction extruded and hot extruded AA2024 studs. J. Mater. Process. Technol. 341, 118862. http://dx.doi.org/10.1016/j.jmatprotec.2025.118862.

Baffari, D., Buffa, G., Campanella, D., Fratini, L., 2017a. Al-SiC metal matrix composite production through friction stir extrusion of aluminum chips. Procedia Eng. 207, 419–424. http://dx.doi.org/10.1016/j.proeng.2017.10.798, International Conference on the Technology of Plasticity, ICTP 2017, 17-22 September 2017, Cambridge, United Kingdom.

Baffari, D., Buffa, G., Campanella, D., Fratini, L., Reynolds, A.P., 2017b. Process mechanics in friction stir extrusion of magnesium alloys chips through experiments and numerical simulation. J. Manuf. Process. 29, 41–49. http://dx.doi.org/10.1016/j.jmapro.2017.07.010.

Baffari, D., Buffa, G., Fratini, L., 2017c. A numerical model for wire integrity prediction in friction stir extrusion of magnesium alloys. J. Mater. Process. Technol. 247, 1–10. http://dx.doi.org/10.1016/j.jmatprotec.2017.04.007.

Bagheri, B., Abbasi, M., Abdolahzadeh, A., Kokabi, A.H., 2020. Numerical analysis of cooling and joining speed effects on friction stir welding by smoothed particle hydrodynamics (SPH). Arch. Appl. Mech. 90, 2275–2296. http://dx.doi.org/10.1007/s00419-020-01720-4.

Behnagh, R.A., Shen, N., Ansari, M.A., Narvan, M., Besharati Givi, M.K., Ding, H., 2015. Experimental analysis and microstructure modeling of friction stir extrusion of magnesium chips. J. Manuf. Sci. Eng. 138 (4), 041008. http://dx.doi.org/10.1115/1.4031281.

Borja, R.I., 2013. J2 plasticity. In: Plasticity: Modeling & Computation. Springer Berlin Heidelberg, Berlin, Heidelberg, pp. 31–58. http://dx.doi.org/10.1007/978-3-642-38547-6_3.

Brar, N.S., Joshi, V.S., Harris, B.W., 2009. Constitutive model constants for Al7075-t651 and Al7075-T6. AIP Conf. Proc. 1195 (1), 945–948.

Chen, G., Zhang, W., Wang, L., Cui, F., 2009. Finite element modeling of friction extrusion process. J. Mater. Process. Technol. 209 (8), 3885–3890.

Cho, J.H., Jae Kim, W., Gil Lee, C., 2014. Texture and microstructure evolution and mechanical properties during friction stir welding of extruded aluminum billets. Mater. Sci. Eng.: A 597, 314–323. http://dx.doi.org/10.1016/j.msea.2013.12.087.

Dhoka, S., Wagner, S.W., Abhi, H., Hendrickson, N.V., Emblom, W.J., 2021. Integrating friction-stir back extrusion to powder metallurgy. V001T02A002. http://dx.doi.org/10.1115/MSEC2021-64052.

Elbossily, A., Kallien, Z., Chafle, R., Fraser, K.A., Afrasiabi, M., Bambach, M., Klusemann, B., 2025. GPU-accelerated meshfree computational framework for modeling the friction surfacing process. Comput. Part. Mech. http://dx.doi.org/10.1007/s40571-025-01048-2.

Feng, Z., David, S.A., Manchiraju, V.K., Frederick, D.A., Thomas, W., 2023. Friction extrusion: Solid-state metal synthesis and recycling in sustainable manufacturing. J. Oper. Manage. 75 (8), 2962–2973. http://dx.doi.org/10.1007/s11837-023-05824-4.

Fraga Filho, C.A.D., Fraga Filho, C.A.D., Castro, 2019. Smoothed Particle Hydrodynamics. Springer, http://dx.doi.org/10.1007/978-3-030-00773-7.

Ghosh, A., 2001. Segregation in cast products. Sadhana 26, 5–24. http://dx.doi.org/10.1007/BF02728476.

Huang, K., Logé, R., 2016. A review of dynamic recrystallization phenomena in metallic materials. Mater. Des. 111, 548–574. http://dx.doi.org/10.1016/j.matdes.2016.09.012.

Jamshidi Aval, H., 2021. Comprehensive thermo-mechanical simulation of friction surfacing of aluminum alloys using smoothed particle hydrodynamics method. Surf. Coat. Technol. 419 (2019), 127274. http://dx.doi.org/10.1016/j.surfcoat.2021.127274.

Johnson, G.R., Cook, W.H., 1983. A constitutive model and data for metals subjected to large strains, high strain rates and high temperatures. In: Proceedings of the 7th International Symposium on Ballistics. pp. 541–547.

Li, L., Escobar, J.D., Das, H., Shukla, S., Schuessler, B.J., Overman, N.R., Grant, G.J., Mathaudhu, S.N., Dos Santos, J.F., Powell, C.A., Soulami, A., 2024. A dislocation density-based meshfree computational framework for solid phase processing. Int. J. Mech. Sci. 267, 108962. http://dx.doi.org/10.1016/j.ijmecsci.2024.108962.

Li, L., Gupta, V., Li, X., Reynolds, A., Grant, G., Soulami, A., 2021a. Meshfree simulation and experimental validation of extreme thermomechanical conditions in friction stir extrusion. Comput. Part. Mech. 8, 1–21. http://dx.doi.org/10.1007/s40571-021-00445-7.

Li, L., Reza-E-Rabby, M., Overman, N., Wang, T., Whalen, S., Grant, G., Mathaudhu, S., Soulami, A., 2022. Analysis of contact conditions and microstructure evolution in shear assisted processing and extrusion using smoothed particle hydrodynamics method. Mater. Des. 221, 111010. http://dx.doi.org/10.1016/j.matdes.2022.111010.

Li, X., Zhou, C., Overman, N., Ma, X., Canfield, N., Kappagantula, K., Schroth, J., Grant, G., 2021b. Copper carbon composite wire with a uniform carbon dispersion made by friction extrusion. J. Manuf. Process. 65, 397–406.

Lin, J., Bao, X., Hou, Y., Min, J., Qu, X., Tao, Z., Chen, J., 2020. Investigation on yield behavior of 7075-T6 aluminum alloy at elevated temperatures. Chin. J. Mech. Eng. 33 (1), 76. http://dx.doi.org/10.1186/s10033-020-00494-8.

Lin, C.N., Tzeng, Y.C., Lee, S.L., Tan, A.H., Fuh, Y.K., Sołek, A.Ł., Lin, C.Y., 2023. Microstructure evolution and Zener-Hollomon parameter analysis as-extruded 7005 aluminum alloy during hot deformation. Mater. Today Commun. 37, 107604. http://dx.doi.org/10.1016/j.mtcomm.2023.107604.

Ma, F., Fu, D., Liu, Y., Yang, D., Zhang, S., Sha, Z., 2020. The numerical simulation of temperature field in friction stir welding of 7075 aluminium alloy. IOP Conf. Ser.: Mater. Sci. Eng. 751, 012081. http://dx.doi.org/10.1088/1757-899X/751/1/012081.

MatWeb, 2025. Online materials information resource. Data used for AA 7075-T6, H13 Tool Steel, and AISI 4140 Steel, URL https://www.matweb.com/. (Accessed 04 March 2025).

Röthlin, M., Klippel, H., Afrasiabi, M., Wegener, K., 2019. Meshless single grain cutting simulations on the GPU. Int. J. Mechatronics Manuf. Syst. 12 (3–4), 272–297. http://dx.doi.org/10.1504/IJMMS.2019.103488.

Saha, P.K., 1998. Thermodynamics and tribology in aluminum extrusion. Wear 218 (2), 179–190. http://dx.doi.org/10.1016/S0043-1648(98)00210-5.

Stubblefield, G., Fraser, K., Phillips, B., Jordon, J., Allison, P., 2021. A meshfree computational framework for the numerical simulation of the solid-state additive manufacturing process, additive friction stir-deposition (AFS-D). Mater. Des. 202, 109514. http://dx.doi.org/10.1016/j.matdes.2021.109514.

Suhuddin, U.F., Rath, L., Halak, R.M., Klusemann, B., 2023. Microstructure evolution and texture development during production of homogeneous fine-grained aluminum wire by friction extrusion. Mater. Charact. 205, 113252. http://dx.doi.org/10.1016/j.matchar.2023.113252.

Tang, W., Reynolds, A., 2010. Production of wire via friction extrusion of aluminum alloy machining chips. J. Mater. Process. Technol. 210 (15), 2231–2237. http://dx.doi.org/10.1016/j.jmatprotec.2010.08.010.

Trimble, D., O'Donnell, G., 2015. Constitutive modelling for elevated temperature flow behaviour of AA7075. Mater. Des. 76, 150–168. http://dx.doi.org/10.1016/j.matdes.2015.03.062.

Whalen, S., Overman, N., Joshi, V., Varga, T., Graff, D., Lavender, C., 2019. Magnesium alloy ZK60 tubing made by shear assisted processing and extrusion (ShAPE). Mater. Sci. Eng.: A 755, 278–288. http://dx.doi.org/10.1016/j.msea.2019.04.013.

William D. Callister, J., Rethwisch, D.G., 2020. Materials Science and Engineering: An Introduction, tenth ed. Wiley, Hoboken, NJ.

Ye, T., Xia, E., Qiu, S., Liu, J., Yue, H., Tang, J., Wu, Y., 2024. Deformation behavior of an extruded 7075 aluminum alloy at elevated temperatures. Materials 17 (5), http://dx.doi.org/10.3390/ma17051210.

Zhang, H., Li, X., Deng, X., Reynolds, A., Sutton, M., 2018. Numerical simulation of friction extrusion process. J. Mater. Process. Technol. 253, 17–26. http://dx.doi.org/10.1016/j.jmatprotec.2017.10.053.

Zhu, D., Zhen, L., Lin, C., Shao, W.Z., 2007. High temperature deformation mechanism of 7075 aluminum alloy. Key Eng. Mater. 353–358, 691–694. http://dx.doi.org/10.4028/www.scientific.net/KEM.353-358.691.

Zou, Y., Li, W., Yang, X., Patel, V., Shen, Z., Chu, Q., Wang, F., Tang, H., Cui, F., Chi, M., 2022. Characterizations of dissimilar refill friction stir spot welding 2219 aluminum alloy joints of unequal thickness. J. Manuf. Process. 79, 91–101. http://dx.doi.org/10.1016/j.jmapro.2022.04.062.